



Measuring polycentric urban development with multi-temporal Sentinel-1 SAR imagery: A case study in Shanghai, China

Xu Zhang^a, Ling Chang^{a,*}, Mingshu Wang^{b,*}, Alfred Stein^a

^a Faculty of Geo-Information Science and Earth Observation (ITC), University of Twente, 7514AE Enschede, The Netherlands

^b School of Geographical & Earth Sciences, University of Glasgow, UK

ARTICLE INFO

Keywords:

Polycentric urban development
Kittler and Illingworth with a modified model (KI-MM)
Sentinel-1
Google Earth Engine

ABSTRACT

Studies on polycentric urban development (PUD) have been done by using LandScan and point of interest data. So far, the quality of PUD products has been limited by the spatio-temporal resolution of these datasets. Using Sentinel-1 SAR missions with a 10 m pixel spacing and a weekly repeat cycle, this study, for the first time, explores the potential of using a time series of Sentinel-1 SAR images for measuring urban polycentricity. In particular, we develop a variance-based filtering method to mitigate speckle noise. We propose the Kittler and Illingworth with a Modified Model (KI-MM) method to accurately identify PUD-related changes. We focus on the mean distance of new-born patches and the mean patch area for a PUD-related change analysis. These allow us to associate SAR tailor-made output with PUDs. The proposed methods were implemented on Google Earth Engine platform using 304 Sentinel-1 SAR images on the city of Shanghai, China, acquired between 2015 and 2018. We have tested 80 distribution models and found that the Laplace distribution is the best model for the KI-MM method. Our results show 2526, 2409, 4232 new-born patches for 2015–2016, 2016–2017, 2017–2018, with areas equal to 18, 20, 36 km², respectively. Using cross-validation with Sentinel-2 (optical) reference, we found that the matching rates and F1-score between detected changes and reference for the years 2015–2016, 2016–2017, 2017–2018 were equal to 89.79% and 91.67%, 100% and 100%, 88.64% and 94.06%, respectively. We conclude that Sentinel-1 SAR images are suited to PUD applications at an intra-city scale with a high spatio-temporal resolution.

1. Introduction

1.1. Polycentric urban development

Over the past decades, polycentric urban development (PUD) has evolved as a key concept in urban planning, as a framework for empirical assessment (Hall and Pain, 2006) and as a strategy for normative development (Bailey and Turok, 2001). Meanwhile, PUD has become a stretched concept, rendering its variations in definition along with its measurement framework (Derudder et al., 2021). The key to PUD is the existence of multiple proximate urban centers, where it lacks an obvious hierarchy (e.g., dominance and connectivity) amongst different centers (Van Nuffel et al., 2010). Despite a proliferation of studies that measure the status of urban polycentricity at different scales, we identify two research trends and possible knowledge gaps. First, following classical polycentricity research with secondary data in pre-defined administrative boundaries, recent studies utilized finer-detailed geospatial information that delineate urban sub-centers with more details. Two prominent examples are grid-based geospatial products

such as LandScan (Liu and Wang, 2016) and point of interest (POI) data based upon crowdsourced data (Liu et al., 2021). Urban centers defined via LandScan benefit from their harmonized production framework for global coverage for more than two decades. Considering their 1 × 1 km² spatial resolution, a detailed and nuanced analysis at an intra-city scale is not feasible. Urban centers extracted from POI data have a detailed spatial resolution, while the crowdsourced nature of POI information may lack the required data quality across different geographical areas and periods. Therefore, PUD research using an analytical framework incorporating data characterized by high spatial and temporal resolution is needed. Second, from an empirical point of view, there is a dearth of studies investigating the dynamics of PUD. For instance, Li and Derudder (2020), and Liu (2020) are so far the only empirical studies focusing on the temporal dynamism of urban polycentricity. To further investigate such an analytical framework, this study, for the first time, investigates the dynamic PUD solution using satellite Synthetic Aperture Radar (SAR) imagery with a high spatio-temporal resolution.

* Corresponding authors.

E-mail addresses: ling.chang@utwente.nl (L. Chang), Mingshu.Wang@glasgow.ac.uk (M. Wang).

<https://doi.org/10.1016/j.jag.2023.103340>

Received 5 October 2022; Received in revised form 27 April 2023; Accepted 29 April 2023

Available online 30 May 2023

1569-8432/© 2023 The Author(s). Published by Elsevier B.V. This is an open access article under the CC BY license (<http://creativecommons.org/licenses/by/4.0/>).

1.2. Synthetic Aperture Radar (SAR) in change detection

Satellite SAR techniques provide a powerful tool to deliver Earth observations for various applications in such as agriculture, forestry, ocean, and hazard (Liu et al., 2019). Thanks to the increase of SAR observations, we can monitor surface dynamics in both time and space (Ban and Yousif, 2012). Although those SAR-based techniques are not straightforwardly designed for the PUD application, we see good possibilities to do so with advanced methods of change detection in SAR imagery.

Change detection in SAR imagery has two facets. (i) Patch-wise change detection, which is based on ground target features where the geometric rectification is more relevant than the radiation correction (Wan et al., 2019). Application examples include sea ice monitoring, glaciers, oceanic features, and other shape-based change detection (Zhao et al., 2022). (ii) Pixel-wise change detection, which considers both the geometric rectification and radiation correction, and its application examples include monitoring crop variation, soil moisture change, and land-use changes (Kumar et al., 2020). By embracing machine learning methods, change detection can be realized by either supervised or unsupervised methods. Supervised methods need ground truth to train the classifier, while unsupervised methods use the pixel information (e.g., spectral, spatial and structure features) to extract the changes automatically (Fang et al., 2022). Unsupervised change detection can be done by algebraic subtraction (Ma et al., 2012), being a simple and straightforward way to get the difference map. The simplicity of this method, however, cannot always secure accuracy, as speckle noise lowers the quality of obtained images. Several other methods are proposed to reduce its impact. Gong (2011) proposed the neighbor-based ratio approach that combines gray level information and spatial information of neighbor pixels. Ma (2012) investigated the wavelet fusion method that fuses the wavelet coefficients for low- and high-frequency bands. Sofiane (2010) put forward the similarity measures method based on pixel intensity or local statistics. These methods, however, do not provide a significant improvement compared with the commonly used log-ratio method (Hu and Ban, 2014). We introduce the ratio change detection method to address this issue.

When using the log-ratio method to derive the difference map, a major challenge is how to define a proper threshold is essential to separate the types of changed areas. Kittler et al. (1984) proposed an automatic threshold algorithm to extract the changed information based on the statistical information of the images. The drawback of this method (Nakagawa and Rosenfeld, 1979) is that the result is sensitive to the correctness of the probability distribution function (PDF) assumption. To tackle this issue, Kittler and Illingworth (1986) proposed KI thresholding, which utilizes statistical decision theory to determine the minimum error threshold, thus overcoming the drawbacks above. KI thresholding has become a common method in determining the threshold. Moser (2006) developed the KI to be a generalized Kittler and Illingworth thresholding (GKIT) method. Hu (2014) applied this GKIT method over large urban areas to detect the changes if the difference map does not follow the unimodal histogram because of the high proportion of changed pixels. Ban (2012) has tested four density functions for urban change detection and validated the efficiency of different models. With the development of the SAR sensors, especially Sentinel-1, however, some assumptions may not hold anymore. For example, changed pixels often count for a relatively small portion w.r.t. the coverage of a Sentinel-1 image, and the distribution model of the difference map varies over time. Hence, this study will further develop the traditional KI thresholding to leverage assumption constraints.

1.3. The use of Google Earth Engine (GEE)

Google Earth Engine (GEE) is designed to deal with the abundance of remote-sensed data, including SAR and optical imagery and the

geospatial analysis of the global scale and large time span (Gorelick et al., 2017; Tamiminia et al., 2020). It provides an online application programming interface (API) to investigate petabyte remote sensing data. Many GEE-related studies have been published recently, such as vegetation monitoring, landcover mapping, agricultural applications, disaster management, and earth science. Only a few PUD-related studies upon the GEE platform are available. These consider investigating the urban growth and urban-rural gradients in the Greater Bay Area (Xie et al., 2022), analyzing the anthropogenic heat flux in monocentric and polycentric cities (Puttanapong et al., 2022), and transformation towards a mega-regional formation (Morshed et al., 2022). More studies and demonstrations in this regard should be done to utilize the capable resource on this platform.

The main contribution of this study is to develop SAR methods for PUD by categorizing ground target changes. The rest of the paper is organized as follows. These methods are demonstrated on the GEE platform using large-scaled high spatio-temporal SAR data in a polycentricity study. Section 2 introduces our KI-MM (Kittler and Illingworth with a Modified Model) threshold determination method and proposes a change-type classification method. Section 3 describes the study area and the data we used. The change detection and validation results are also presented in Section 3, followed by discussion and conclusions in Section 4 and Section 5, respectively.

2. Methods

We introduce the three-block data processing flowchart in Section 2.1 and elucidate the methods employed during data processing. Next, we introduce an adapted log-ratio method, called KI-MM (Kittler and Illingworth with a Modified Model) specifically, for various difference maps in Section 2.2. Then, we describe a threshold segmentation method to separate changed and unchanged pixels in Section 2.3. Finally, Section 2.4, presents a method to reclassify the changed pixels according to the proposed classification metrics.

2.1. Processing flowchart

The processing flowchart includes three blocks: 1. *preprocessing*, 2. *change detection* and 3. *postprocessing*, as shown in Fig. 1.

1. *Preprocessing*: On the GEE platform the SAR amplitude time series are loaded and analyzed to detect the changes between SAR acquisitions. SAR images are first mosaicked when multiple SAR scenes cover the whole area of interest (AOI). Next, temporal averaging is applied on all SAR images in each stack to mitigate noise and impact due to temporal decorrelation. Then an external shapefile can be used to crop the stitched SAR images to the AOI. Spatial smoothing using, e.g., morphological mean filter (Lin et al., 2016), Lee filter (Rubel et al., 2021) can be applied to reduce speckle noise influence further. As an optional step, *a priori* knowledge, e.g., the optical images used to produce the NDVI-NDWI masks, is employed to exclude the vegetation areas and water bodies (Szabo et al., 2016).

2. *Change detection*: We designed the KI-MM (Kittler and Illingworth with a Modified Model) method to detect any changed pixels in this section. The key step of the KI-MM method is to find the optimal distribution model of the derived pixel-wise ratio map (details in Section 2.2), and integrate the distribution model with the threshold criterion function $J(T)$ (see Section 2.3). The KI-MM method minimizes $J(T)$ to determine the best threshold K_{KI} for class separation, akin to traditional KI. Then, for each D_{LR} in the pixel-wise ratio map, it will fall into changed or unchanged categories in accordance with the K_{KI} .

3. *Postprocessing*: A patch is considered to be discarded if its area is below the predefined threshold K_{Area} . K_{Area} is defined based on the knowledge of noise level and minimal expected changed area size. After refining the changed area, we classify the changed areas based on the inequality $S_{GEEb} - S_{GEEa} = D$ (Eq. (6)) into positive change ($D > K_+$), negative change ($D < K_-$) and stable area ($D = K_d \pm e$, stable area means no ground change between two time spots), where K_+ is the positive K_{KI} , K_- is the negative K_{KI} (refer to Fig. 5 (d)), and e is the acceptable stochastic variation.

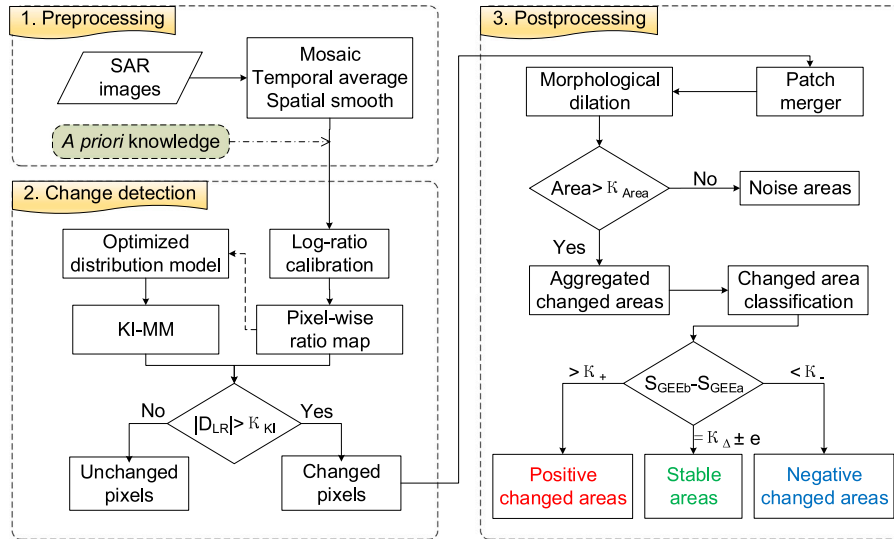


Fig. 1. Processing flowchart.

2.2. Log-ratio

The intensity value of pixel at position (x, y) in two SAR image stacks, denoted as $I_A(x, y)$, $I_B(x, y)$. Every image stack includes a group of images, which are lumped together annually for our case. For instance, one stack covers images acquired in 2015 while the other one covers images acquired in 2016. Then $I_A(x, y)$ being temporally-averaged intensities of image stack A is obtained as

$$I_A(x, y) = \frac{\sum_i^{m_a} I_a(x, y)}{m_a}, \quad (1)$$

where m_a represents the number of SAR acquisitions, $I_a(x, y)$ indicates the intensity value of the pixel at position (x, y) for the i th acquisition. A similar expression applies to stack B.

The pixel-wise log-ratio is employed to differentiate the changed areas from unchanged areas in SAR intensity maps, expressed as (Kittler and Illingworth, 1986)

$$D_{LR}(x, y) = \log_{10} \frac{I_B(x, y)}{I_A(x, y)}, \quad (2)$$

where $D_{LR}(x, y)$ represents the log-ratio at the pixel position (x, y) . In Eq. (2), the ratio is first taken between the intensity value of the corresponding pixel at position (x, y) in two SAR image stacks, and then converted into the logarithmic domain.

Considering the format disparity between raw and pre-processed SAR images on GEE, $I_A(x, y) = 10^{\frac{S_{GEEa}(x, y)}{10}}$ and a similar expression applies to $S_{GEEb}(x, y)$. Then $D_{LR}(x, y)$ can be reformulated as

$$D_{LR}(x, y) = \frac{1}{10} (S_{GEEb}(x, y) - S_{GEEa}(x, y)). \quad (3)$$

Here, $S_{GEEa}(x, y)$ and $S_{GEEb}(x, y)$ are the intensity at position (x, y) in the logarithmic domain for image stack A and B on the GEE platform, respectively.

2.3. KI with the modified model

Determining the appropriate critical values for D_{LR} is important to distinguish between changed and non-changed areas. Here we review and further develop upon the minimum error thresholding method, KI thresholding, which is developed by Kittler and Illingworth (Kittler and Illingworth, 1986).

Using Eq. (3), the log-ratio map of SAR image stacks A and B, being a gray scale map, can be obtained. The histogram of this log-ratio map, $h(X)$ from the observations X , is equal to a mixture of changed

or unchanged areas. Each observation can be denoted as potential threshold T to separate these two classes, but, not all of T is the best threshold value K_{KI} at a global scale. We define the criterion function $J(T)$ to identify the best threshold value K_{KI} among all the potential thresholds T , expressed as

$$J(T) = - \sum h(X) \ln[h(X|c, T)P_c(T)], \quad (4)$$

where $J(T)$ represents the quality of the threshold T , c indicates the class index, e.g., $c \in \{1, 2\}$, $h(X|c, T)$ is the best fitting distribution model for the log-ratio map, and $P_c(T)$ is the prior probability density function (PDF). The lowest value of $J(T)$ corresponds with the optimized threshold K_{KI} . Therefore, the best critical value K_{KI} for D_{LR} is determined by $K_{KI} = \text{argmin}_T J(T)$, $T \in \{X\}$.

Traditional KI thresholding uses the Normal distribution model to shape $h(X|c, T)$. The Normal distribution kernel, however, cannot well represent all the log-ratio maps because of the familiar bell curve shape and moderate slope. The histogram of log-ratio maps is pointed in the middle, like a pole holding up a circus tent, and has sharp slopes. The SAR image change detection differs from the optical image since the SAR amplitude image is often supposed to follow the Rayleigh distribution (Kuruoglu and Zerubia, 2004). Ban and Yousif (2012) demonstrated that the SAR change map is more suitable for the Laplace, Log normal, or Nakagami ratio distribution model. In practice, we observe that the magnitude of the SAR images will vary because of different SAR sensors, and the reflectivity of variational ground truth may change for the same sensor. Therefore, a suitable distribution model should be evaluated for different scenarios. Here we propose a Kittler and Illingworth with a Modified Model (KI-MM) to replace the distribution model $h(X|c, T)$ with a best-fitted model. To be more specific, we test the difference maps with commonly used distribution models listed in Scipy (Virtanen et al., 2020). For this study, the Laplace distribution model is the best-filled model, formed as $f(X|u, b) = \frac{1}{2b} \exp(-\frac{|X-u|}{b})$, where $b = \frac{1}{N} \sum_m^n |X - u|$, $X \in [m, n]$, $[m, n]$ is the bound of the log-ratio map, N is the total number of log-ratio pixels, and u is the mean value. For this model we substitute $h(X|c, T)$ and derive the criterion function $J(T)$ with class index $c \in \{1, 2\}$ (see in A), where $J(T)$ equals

$$J(T) = P_1 \ln 2b_1 + P_1(T) \sum_m^n \frac{|X - u_1(T)|}{b_1} - P_1(T) \ln(P_1(T)) \\ + P_2 \ln 2b_2 + P_2(T) \sum_m^n \frac{|X - u_2(T)|}{b_2} - P_1(T) \ln(P_2(T)), \quad (5)$$

and summations \sum cover the different classes of the histogram.

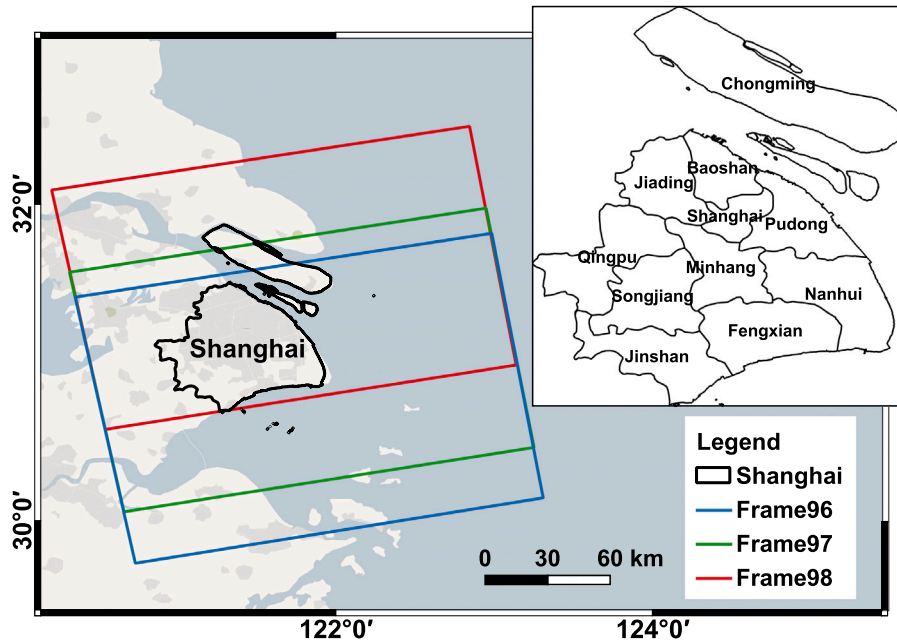


Fig. 2. Study area and SAR image coverage.

2.4. Change type classification

The areas labeled by $c = 1$ and $c = 2$ are classified by a log-ratio classification and by KI-MM thresholding. We now consider that the polycentric urban development manifests itself as positive and negative changes. By analyzing the intensity difference between stack A and B, denoted as D , we classify the change type by

$$D = S_{GEEb} - S_{GEEa} \begin{cases} > K_+, \text{ positive} \\ < K_-, \text{ negative} \\ = K_d \pm e, \text{ neutral} \end{cases} \quad (6)$$

where e is the allowable bias or predefined tolerance. A negative change, $D < K_-$, implies that the intensity value (in decibels) of a pixel decreases in image stack B from the corresponding value in image stack A. A positive change, $D > K_+$, indicates that the intensity value of a pixel increases in image stack B from the value in image stack A. When $D = K_d \pm e$, no change occurs. In a noise-free scenario, e equals to zero. For instance, if a ground target, e.g., a single building, appears in image stack A and is absent in image stack B, then the intensity value decreases and $D < K_-$, thereby indicating a negative change. If a building exists in image stack B but not in image stack A, then the intensity value increases and $D > K_+$, thereby indicating a positive change. The positive change is regarded as new-born patch or city center in later analysis. If a building exists in both stack A and B, then $D = K_d \pm e$, no change occurs.

2.5. PUD indicators

To facilitate SAR-derived positive changes for the polycentric urban development monitoring, we propose two indicators, (i) patch mean distance and (ii) patch area. (i) Patch mean distance is the average distance between the nearest patches. To obtain the mean distance M_{dis} , one first identifies the nearest patches, then calculates the distance between the patch boundary of every two patches, and computes the average distance of all patches. M_{dis} is obtained by

$$M_{dis} = \frac{2 \sum Dis(Area_i, Area_j)}{N_{Area}(N_{Area} - 1)}, \quad (7)$$

where $Dis()$ is the distance between patches $Area_i$ and $Area_j$ ($i, j \in [1, N_{Area}]$ but $i \neq j$) and N_{Area} ($N_{Area} \geq 2$) is the total number

of calculated patches. The standard deviation of patch mean distance (STD) equals

$$STD = \sqrt{\frac{\sum (Dis(Area_i, Area_j) - M_{dis})^2}{N_{Area}}}, \quad (8)$$

reflecting the degree of concentration. (ii) Patch area, is an important indicator in describing city centers (Hajrasouliha and Hamidi, 2017). It is expressed as

$$M_{Area} = \frac{\sum_{i=1}^{N_{Area}} Area_i}{N_{Area}}, \quad (9)$$

showing the mean spatial extent of all changed patches.

3. Experiments and results

3.1. Study area: the city Shanghai

The test site covers the city of Shanghai city, China, outlined in black in Fig. 2. This study area is interesting for our proposed method from empirical and planning perspectives. Situated in the Yangtze River Delta megaregion, it embodies a high degree of both inter-city polycentricity and intra-city polycentricity (Liu and Wang, 2016; Liu et al., 2018). Shanghai is a *de facto* polycentric city with several different data sources and measurement schemes (Zhang et al., 2019). It has explicitly adopted the PUD strategy for its economic growth and industrial restructuring (Murakami and Chang, 2018). For instance, its municipal government sequentially decided to establish new employment sub-centers (named “mini-CBDs”) surrounding the traditional city center in 2006, 2007, and 2012, primarily by converting former industrial parks or upgrading old commercial districts along with floor area ratio increases, transportation infrastructure investments, and land use right sales for new commercial estate development. PUD strategies have been formulated as “1+8” (one CBD, eight subcenters) and as “1+8+60” (one CBD, eight new centers, 60 satellite towns). More recently, Shanghai has put forward a more ambitious vision for urban polycentricity in its 2030 master plan (Chen, 2014).

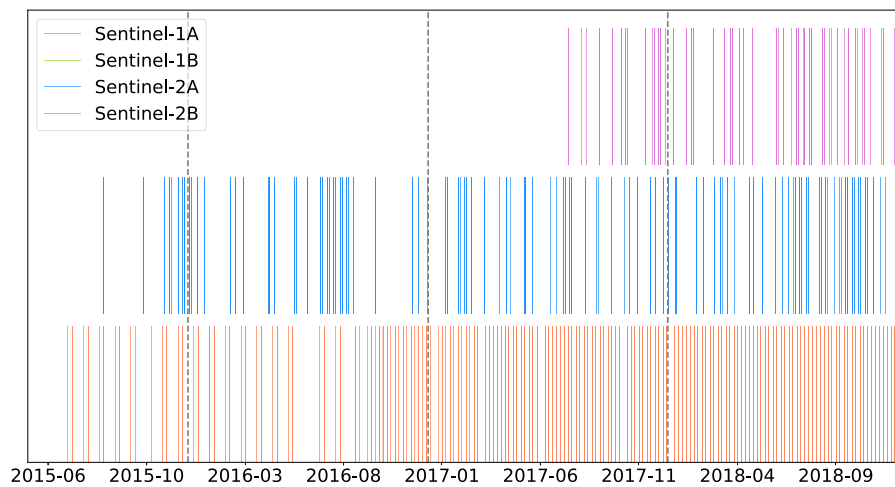


Fig. 3. Sentinel-1A/B and Sentinel-2A/B acquisition information. The dashed lines separate the images in terms of years.

3.2. Sentinel-1 and Sentinel-2 data

We used Sentinel-1A/B SAR ground range detection (GRD) data in C-band. Sentinel-1A/B SAR satellites offer high-temporal sampling data with a 6-day repeat cycle, and are operated in either VV and VH or HH and HV polarization channels. Specifically, our data have a 10 m pixel spacing in IW mode and VH channel on GEE platform. All Sentinel-1A/B images (as shown in red and green in Fig. 3, respectively) were acquired between 2015 and 2018 in ascending mode. The annual acquisitions equaled 21, 57, 108, and 118, respectively (Fig. 3). As Sentinel-1B data were accessible from September 2016, the total amount of Sentinel-1A/B in the first two years was relatively small. Three frames labeled 96, 97, and 98 were used (Fig. 2).

Sentinel-2A/B data were used as prior knowledge to produce the NDVI-NDWI mask and also used for validation. Bands 3, 4, 8 were used to derive the NDVI-NDWI masks, and bands 2, 3, 4 of a 10 m resolution were fused as true-color images to validate change detection results. Sentinel-2 A data were acquired from June 2015 with ten days repeat cycle, while Sentinel-2B data were acquired from March 2017 and were combined with the Sentinel-2 A to obtain a constellation of five days repeat cycle. In total, we collected 39, 127, 124, and 233 Sentinel-2A/B images in 2015, 2016, 2017, and 2018, respectively, shown in blue and purple in Fig. 3.

3.3. LandScan population data

LandScan High-Resolution Global Population Dataset (Dobson et al., 2000) aggregates various data sources. It provides global population coverage at a 1 km spatial resolution annually. Although its algorithms are still within patent protection, the quality of population estimation has been proven reasonable; LandScan data have been widely applied in dozens of studies and can even be used as the ground truth to validate population distributions (Bhaduri et al., 2007). LandScan provides us with population distribution information at fine resolution, while it also will enable us with potential (international) comparison studies in the future. LandScan data have been widely applied to identify population centers in PUD (Liu and Wang, 2016; Wang et al., 2019; Meng et al., 2021; Wang, 2021; Li and Derudder, 2022).

3.4. Data preprocessing on GEE

Using the GEE platform, all 304 Sentinel-1A/B SAR and 523 Sentinel-2A/B images were preprocessed following block 1. *preprocessing* in the data processing flowchart (Fig. 1).

Intensity time series of all pixels in Sentinel-1A/B were collected on GEE. As an example, Fig. 4 shows the intensity time series in dB of

points P1 (in red), P2 (in blue), and P3 (in green), which were averaged by their patches. The location of these three points is indicated in Fig. 8 (g). We used yearly mean values of the Sentinel-1A/B intensity time series (shown in the dashed line in Fig. 4 as an example) to detect annual changes per point. To reduce the speckle noise, we used a convolution kernel with a radius of 100 pixels. For temporal filtering, we used yearly averaged SAR images and their mean values to detect annual changes. As such, the speckle noise was mitigated. For instance, for the 21 SAR images in 2015, we assumed that every SAR image had the same standard variance σ_{SAR} , the standard error of the annually-averaged SAR for 2015 was equal to $\sigma_{\text{SAR}}/\sqrt{21}$.

We defined the cloud occupancy as $\leq 10\%$ to minimize the influence of the cloud on Sentinel-2A/B. The annual median values of Sentinel-2A/B were computed to mitigate noise. Bands 4 and 8 of Sentinel-2A/B were selected to obtain $\text{NDVI} = \frac{\text{band8} - \text{band4}}{\text{band8} + \text{band4}}$, while bands 3 and 8 were used to derive $\text{NDWI} = \frac{\text{band3} - \text{band8}}{\text{band3} + \text{band8}}$. The pixels, with the NDVI values above 0.1 and NDWI values below 0, were regarded as vegetation and water area, respectively (Ashok et al., 2021), and were binarized as the NDVI-NDWI mask for the preprocessed SAR images.

3.5. Change detection and postprocessing results

According to the procedure in block 2, *change detection*, we used the log-ratio (Eq. (3)) to further analyze the preprocessed SAR stacks. Three ratio maps were generated in a daisy-chain manner between 2015 and 2018. By visually interpreting the histograms of these three ratio maps in Figs. 5(a)–(c), we found that the changed and unchanged pixel values were mixed to form a unimodal histogram. Using the K-MM method, we tested 80 commonly used distribution models with criterion metric including a summation of squared error (SSE). The top three distribution models with minimum SSE values in Table 1 and visualized in Figs. 5(a)–(c). We found that SSE values vary between different yearly ratio maps in Table 1, the best-fitted model is the Laplace distribution with the minimum SSE of 5.75, 3.95, and 6.43 for 2015–2016, 2016–2017, and 2017–2018, respectively. This is followed by Logistic and Normal distribution. Figs. 5(a)–(c) show that the Laplace distribution fits the histograms best. Next, we moved to the change detection threshold selection. Updating Eq. (4) with parameters of the Laplace distribution, we derived Eq. (5) obtaining the threshold quality value $J(T)$, as shown in Fig. 5(d). The $J(T)$ values decrease towards the dip between $(-0.5, 0)$ and increase rapidly to the peak at zero, while for positive T values, the contrary is the case. In the sequel, two local minima on the positive and negative sides served as thresholds to separate the positive and negative changes according to Eq. (6). The final threshold values were equal to -0.157 and 0.142 for SAR image

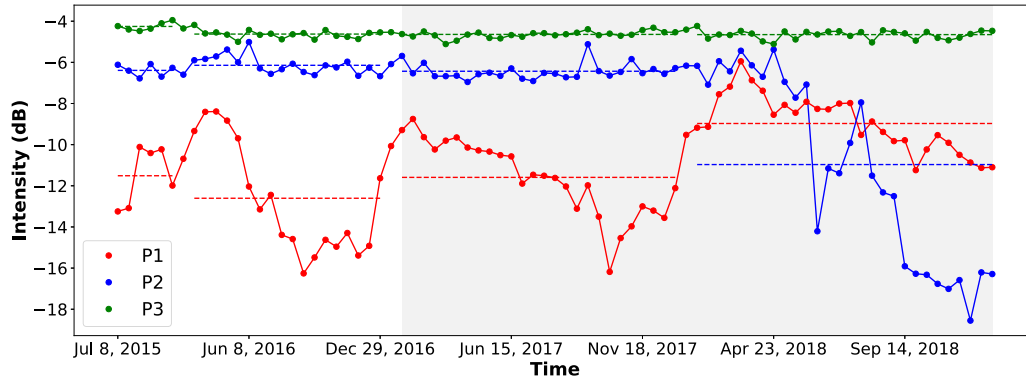


Fig. 4. Intensity time series of three example points P1, P2, P3 (shown in Fig. 8 (g)), in Sentinel-1 images on the GEE platform. The dotted line in red represents the intensity value of P1 in each SAR image acquisition, while blue and green lines represent P2 and P3. The dashed lines represent averaged intensity value of points P1, P2, P3 in 2015, 2016, 2017, and 2018 separately. The gray shade covers the years 2017 and 2018. (For interpretation of the references to color in this figure legend, the reader is referred to the web version of this article.)

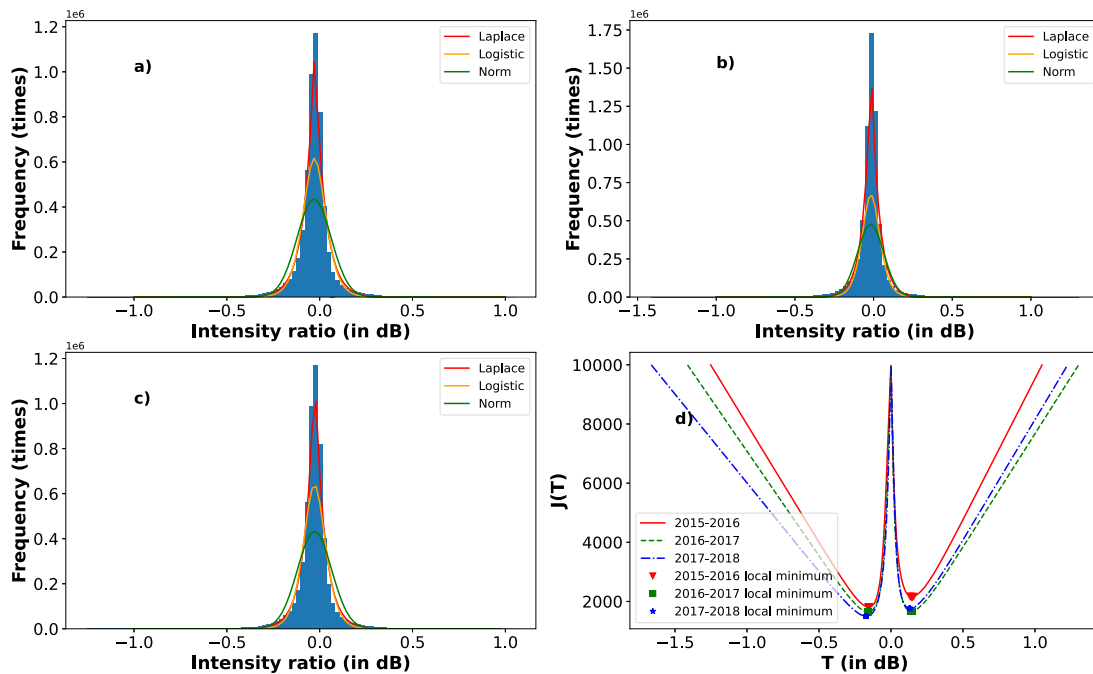


Fig. 5. Histogram of ratio map with the top 3 fitted models of 2015–2016 (a), 2016–2017 (b), 2017–2018 (c), and all potential threshold quality values $J(T)$ (d).

Table 1
The summary of squared error (SSE) of different distribution models in each yearly ratio map (unit: times²).

Distribution model	Laplace	Logistic	Norm
2015–2016	5.75	22.13	56.91
2016–2017	3.95	19.29	50.39
2017–2018	6.43	23.31	58.01

stack 2015 and 2016, -0.163 and 0.137 for 2016 and 2017, -0.175 and 0.129 for 2017 and 2018, respectively.

We then moved to block 3, *postprocessing*. As the detected changed areas occurred irregularly, we applied the following refinement processes to match them with the ground truth. First, patches sharing the same boundary were merged into a larger patch. Acknowledging

that some pixels disappeared in homogeneous patches during the pixel-based change detection, we used a morphological dilation to probe and extend the shapes in the patches. Besides, pixel-based change detection was smeared by the changes of speckle noise, which occurred as isolated (small) patches. These patches were excluded manually by setting an area-size threshold. Considering the 10 m pixel resolution of Sentinel-2 data, we discarded the patches with a spatial extent $\leq 0.005 \text{ km}^2$. As a result, the total number of patches between 2015 and 2016 was equal to 99215, and the area to 364 km^2 , to 107733 and 489 km^2 between 2016 and 2017 and to 118113 and 520 km^2 between 2017 and 2018, respectively (Table 2).

To link the change maps with the PUD, we classified the changed areas into positive, negative changes, and stable areas as described in Section 2.4. For instance, a newly built structure possesses a positive value in the log-ratio map, derived from image stacks in 2015 and 2016.

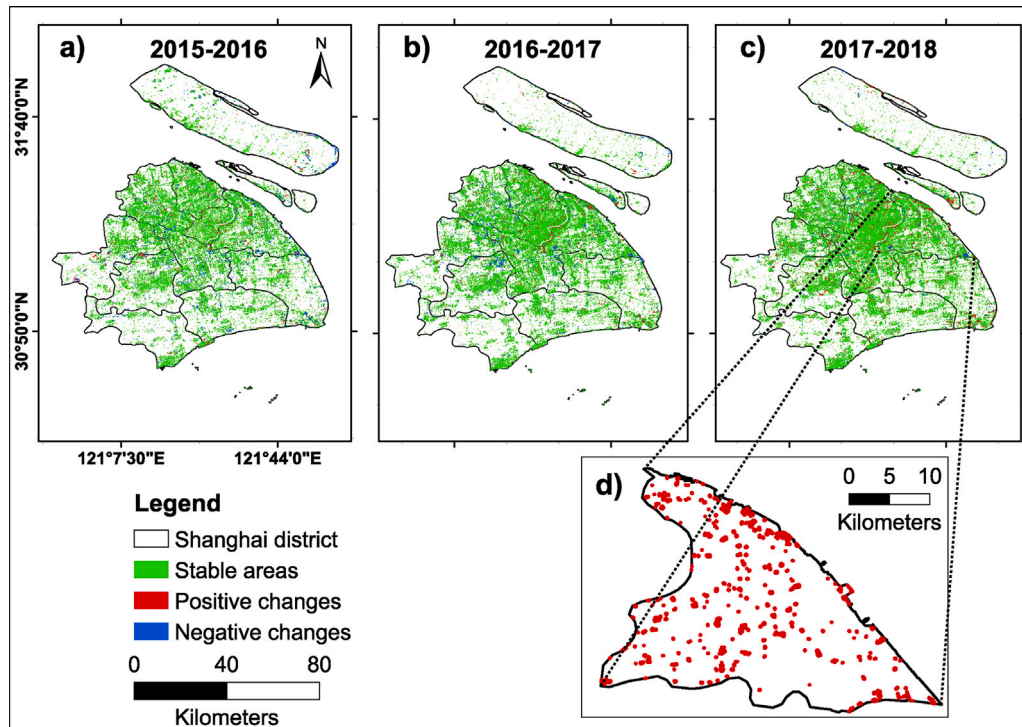


Fig. 6. Change map of 2015–2016 (a), 2016–2017 (b), 2017–2018 (c), and a zoom-in map (d). The positive, negative changes, and stable areas are respectively indicated in red, blue, and green. Only positive change is indicated in (d). (For interpretation of the references to color in this figure legend, the reader is referred to the web version of this article.)

Table 2
The statistical information of changed areas.

Year	Type	Stable areas	Positive changes	Negative changes	Total
2015–2016	Patch number	90869	2526	5820	99215
	Area (km ²)	314	18	32	364
2016–2017	Patch number	100722	2409	4602	107733
	Area (km ²)	439	20	30	489
2017–2018	Patch number	111335	4232	2546	118113
	Area (km ²)	464	36	20	520

Next, we identified positive and negative changes, and stable areas following Eq. (6). Based on Fig. 6, we found that most patches were stable areas, which means these patches remain to be unchanged. Positive and negative change areas were detected in a scattered pattern. Patches with positive and negative changes count for 8.38%, 6.51%, 5.74% of the total number of detected patches between 2015 to 2018, and they are unrecognizable from Fig. 6. Zooming in on the Pudong district in Fig. 6(d), we found that the number of patches increased as well as their spatial extent. There were 325 positive increased patches with an area of 3.02 km² between 2015 and 2016, 342 and 4.11 km² in 2016 and 2017, 618 and 6.24 km² in 2017 and 2018. In this way, we obtained the annual growth rate of new-born city centers, e.g., 42.78% for the Pudong district.

3.6. Validation results

As the LandScan population data were available at a local scale, we selected nine test sites to compare the changed patches by visual interpretation. For each ratio map, three 5.5×5.5 km sites were selected according to the annual changes in the population data. They were located in the high population density area (Fig. 7(a)), while the detected patches in Fig. 7(b) are the results of the change detection experiment based on Sentinel-1. A group of manually selected validation

samples from Sentinel-2 is presented in Fig. 7(c). Acknowledging the disparity in detected-patch patterns between Sentinel-1 and Sentinel-2, we considered that the Sentinel-1 results were in line with the Sentinel-2 reference when the interpreted patches could totally cover or partly cover the Sentinel-1 detected patches. For instance, patch D4 in Fig. 8(f) is fully covered with the validation polygon, while patch D1 in Fig. 8 (d) is only partly covered. In Fig. 8(b), the accuracy of the positive change is obtained using the three correctly classified patch areas (excluding the two patches on the top right), divided by the total detected positive change area. The matching rate for each change type area was presented as the ratio between the corrected patch area and the full area. Following this metric, all three types of change were validated for these nine validation sites (Fig. 8, Table 3). We also calculated the conventional accuracy metric F1-score in Table B.5 in Appendix B, which manifests the same relationship between different types of changes for the selected nine sites.

We found that matching rate values are relatively high except for the positive change in A2 during 2015–2016. Because most of the detected positive patches were containers near the port, they are likely to have changed frequently in time series and are easily misjudged if our SAR image and reference optical image are acquired at different times. The other matching rates all exceed 80%, and even five positives,

Table 3

Validation statistics of the nine validation sites. Here the columns for Positive changes, Negative changes, Stable and average, and the last row for Average show the matching rate between Sentinel-1 and Sentinel-2 results with the units of %.

Year	Validation sites	Positive changes (%)	Negative changes (%)	Stable (%)	Average (%)
2015–2016	A1	100	100	98.26	99.42
	A2	69.36	87.94	96.78	84.69
	A3	100	100	90.16	96.72
2016–2017	B1	100	100	90.54	96.85
	B2	100	92.06	76.48	89.51
	B3	100	98.34	97.31	98.55
2017–2018	C1	93.65	100	98.89	97.51
	C2	83.76	100	99.18	95.98
	C3	88.52	100	95.39	94.64
Average (%)		92.81	97.59	93.66	

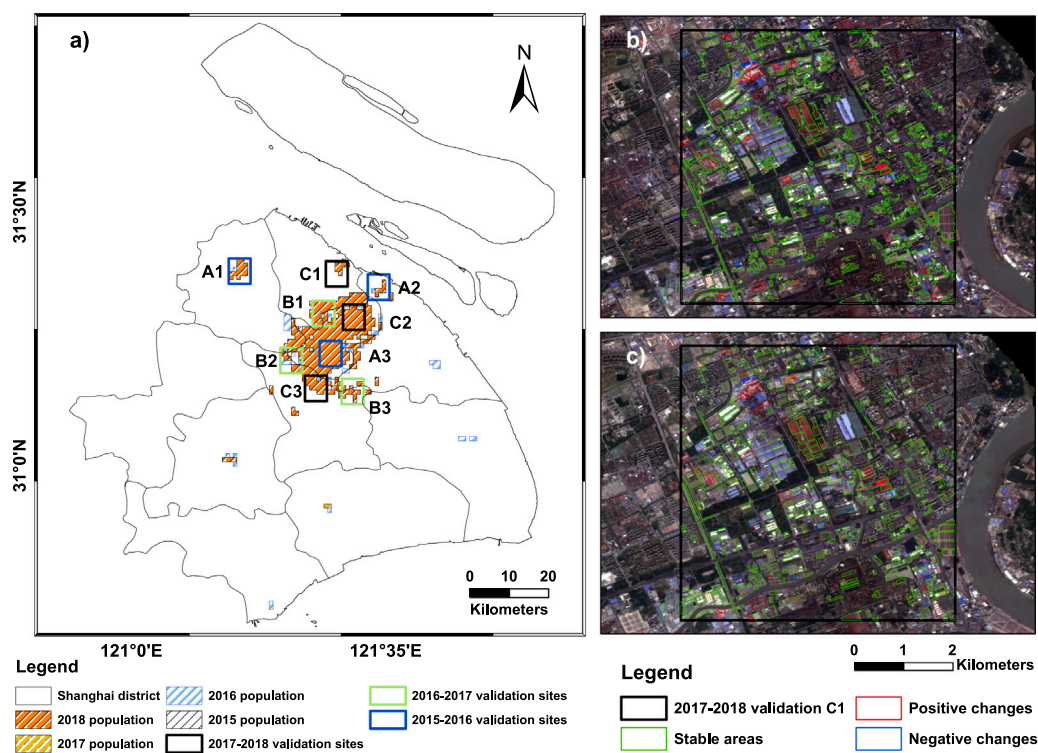


Fig. 7. (a) Validations site map with LandScan population data. (b) Sentinel-1 change detection results superimposed by the 2017 Sentinel-2 image. (c) Visualized interpretation result superimposed by 2018 Sentinel-2 optical image.

six negative matching rates are 100% matching. The positive changed patch number for A1, B1-3 are 5, 11, 5, 1, and negative changed patch numbers for A1, A3, B1, and C1-3 are 1, 1, 4, 10, 1, 4. Note that the matching rate can be high if few changes occurred and all these changes are identified. These limited patch numbers and gentle changes in the inland region compared with rapid changes near the port region did not largely affect the detection results. Overall, for each change type, their average matching rate is above 90%, and for three test sites each year, the average matching rate exceeds 90% except for test site A2 between 2015 and 2016.

To exemplify the relation between the ground truth and Sentinel-1 change detection results, we chose three points, P1, P2, and P3, in Fig. 8. Their intensity time series are shown in Fig. 4. We found that the intensity values of P1 increased from October 2017 to April 2018. This increase could respond to the detected positive changes of this patch between 2017 and 2018 (shown in gray). The intensity values of

P2 are relatively stable until May 2018. There is a sudden decline from May to the end of 2018. Although a small jump occurred between June and August, the decreasing tendency is pronounced. This time series trend resonates with the detected negative changes over this patch. The intensity time series of P3 remains stable, which coincides with the detected stable patch shown in Fig. 8 (g).

3.7. Inner-relation indicators

Mean distances in the nine validation sites are shown in Table 4. They vary from 400 m to 1600 m, except for B3. One isolated positive change patch is observed in this test site, without neighbors, and hence the mean distance closes to zero. Considering the STD of mean distance, almost all STD values are smaller than the mean distance except for the B2 test site. The reason is that three positive changes are concentrated in the top left corner, and one distinguished patch is situated in the

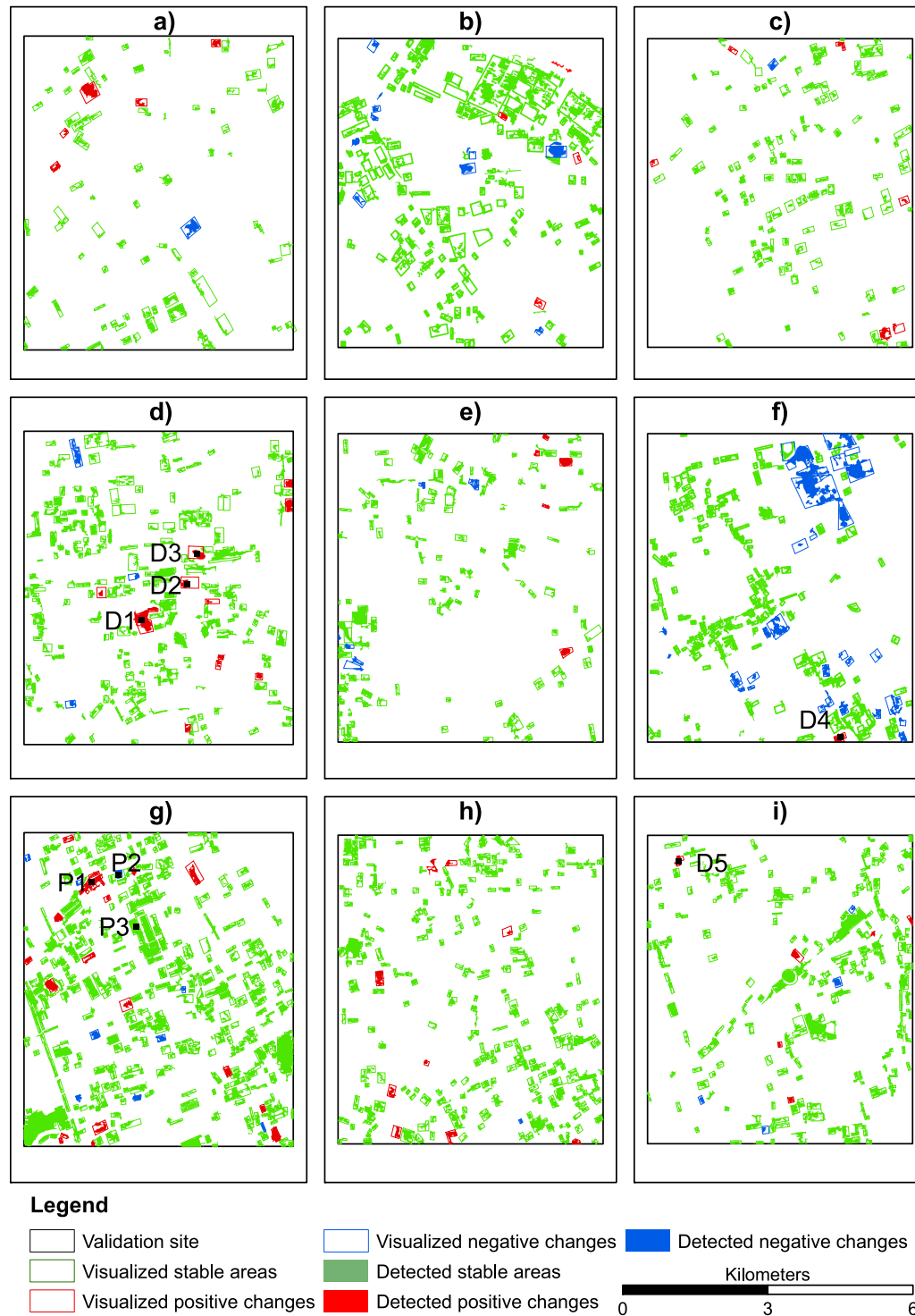


Fig. 8. Validation maps of sites A1 (a), A2 (b), A3 (c), between 2015 and 2016, B1 (d), B2 (e), B3 (f) between 2016 and 2017, and C1 (g), C2 (h), C3 (i) between 2017 and 2018.

bottom right (Fig. 8 (e)). The smaller mean distance indicates that the changes are close, while the minor STD means concentrated distribution of these changes. As a result, the mean distance and STD indicators can reflect the spatial distribution of positive changes (new-born city centers).

Table 4 shows that all the test sites have the minimum patch area values between 5000 m² and 7000 m² except B3. Maximum patch areas

vary a lot, from 15478 m² to 115075 m², caused by different ground change processes. For example, the largest positive change area is located in test site B1, which is a new-born community named Jinganfu, as shown in Fig. 9 (e). In contrast, the minimum value in maximum patch area indicator in test site A2 is caused by containers change in the port region. That is to say, the minimum and maximum patch area can reflect different ground truth variations. The last indicator,

Table 4
Mean distance, patch area, and number of the positive changed patches.

Year	Validation sites	Mean distance (m)	STD of mean distance (m)	Minimum patch area (m ²)	Maximum patch area (m ²)	Mean patch area (m ²)	Patch number
2015–2016	A1	893	473	7017	69637	26070	5
	A2	1243	1104	5631	15478	10239	5
	A3	1609	1116	6397	31756	12134	6
2016–2017	B1	452	382	5851	115075	25839	11
	B2	964	1017	7128	37524	17313	5
	B3	0	0	31729	31729	31729	1
2017–2018	C1	443	358	5009	70960	21806	18
	C2	1048	742	5806	39479	17866	9
	C3	1341	774	5846	21871	12220	6

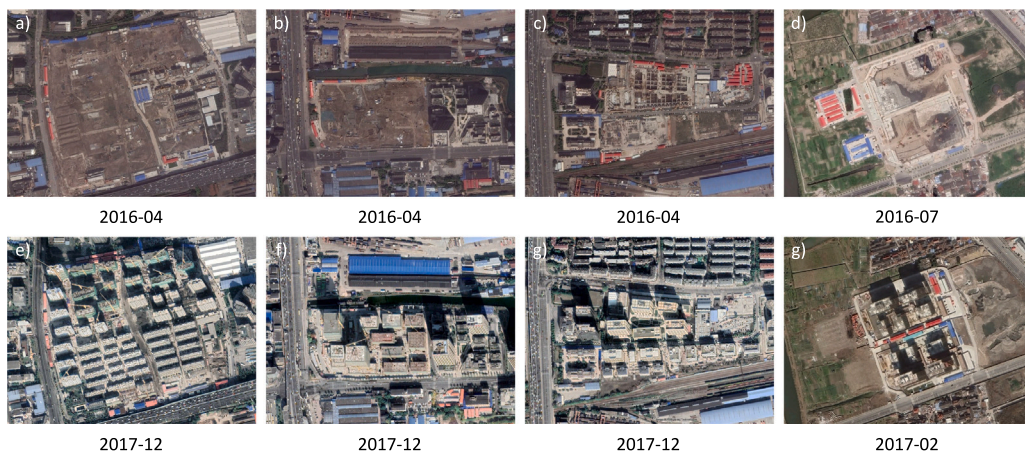


Fig. 9. The pictures of ground truth. (a) Jingnanfu community, (b) Jingnanying community, (c) Xingfukongjian office building, and (d) Sanlin park of Pudong software part are taken in 2016, while (e)–(g) are the corresponding ground truths taken in 2017.

Source: All pictures are taken from Google Earth.

the mean patch area, shows the volume of positive changes with an interval between 0.012 km² and 0.026 km².

4. Discussion

In this section, we discuss the results in comparison of LandScan and SAR data, and the multi-perspective of the observed PUD parameters.

4.1. Results comparison between LandScan and SAR data

As the SAR-based city center detection method can provide the changes in buildings as we showed in Section 3, but not changes in the population, we can synergize both SAR and LandScan data towards operational monitoring of polycentricity development.

Fig. 7 (a) shows that the city centers detected by LandScan data are gathered in Shanghai's main district as the main city center. Nine sub-centers are separately located around it, including Baoshan, Jiading-Anting, Qingpu, Songjiang, Minhang, Fengxian, Jinshan, Lingang, and Chongming. The spatial morphology of the city center corresponds with the master plan designed by Shanghai municipal government, feathering one central city, nine satellite cities, 60 new towns, and 600 key settlements (Liu and Wang, 2016). Because of the 1 km spatial resolution of LandScan data, only nine satellite cities could be observed. Thanks to the higher resolution of SAR data, we can get more information about the 60 new towns and 600 key settlements. For instance, the Jingnanfu community, located in Pinglu Road No. 999, was built in 2018. It was detected in the middle of Fig. 8(d), the biggest patch D1

in red. The corresponding high-resolution optical images (30 cm) are shown in Figs. 9(a) and (e), acquired in different time slots showing the variation from bare ground to built-up community. The nearest patch D2 in the northeast is the Jingnanying community (Figs. 9(b) and (f)), which was under construction and detected between 2016 and 2017. Besides the newly built community, the Xingfukongjian office building (Figs. 9(c) and (g)) was detected on the top of the Jingnanying community as D3. Until July 2021, the occupancy rate of this building reached 90%. This occupancy rate can be used to reflect employment rate, being an important PUD indicator (Chen et al., 2021). In addition, the Sanlin park of the Pudong software park (Figs. 9(d) and (h)) was detected as patch D4 at the bottom of Fig. 8(f). The office building type and the software park were related to the employment trend or employment center index of polycentricity, which could be analyzed in the future, following Zhang (2019), and Sun and Lv (2020). With the combined insight into the population and building changes, we can better understand polycentricity in satellite city and local building change scales.

There is a slight change of the LandScan results when comparing the individual years, as shown in Fig. 7(a). City centers detected by LandScan in 2015 coincide with the centers detected in 2016. Between 2016 and 2017, the centers in Pudong, Nanhui, and Jinshan disappeared while three new centers were born. One of the new-born centers was located in the eastern part of Baoshan. The other two were located in the western part of Minhang. A single change appeared between 2017 and 2018, as a center disappeared in the western part of Fengxian. Since LandScan data are annual data, we aggregated the SAR data to have the same temporal resolution by calculating the mean value of

image stacks in each year. They are shown in Fig. 4 in dotted lines. For example, the detected red patch on the northwest corner in Fig. 8 (i) D5, named Yunbai center, was completed in 2018, but it was also detected as 'under construction' from 2015 to 2017. Because of the six days revisit cycle of the SAR data, we detected more change details (can be reflected by the fluctuated solid lines in Fig. 4) at higher temporal resolution. Then the LandScan and SAR data can be complementary.

4.2. Multi-perspective of monitoring polycentric urban development

When monitoring polycentric urban development on the intra-city scale, various kinds of geospatial data have been used in PUD, like population censuses and economic data (McMillen, 2001), nighttime light satellite images with social media data (Cai et al., 2017), pick-up and drop-off points from taxi GPS data (Wei et al., 2020) land use information (Wang and Debbage, 2021), and commuting flows (Wu et al., 2021). As a result, the main city center and sub-centers were identified. Unlike these traditional methods, our method provides a detailed perspective of urban structure within the intra-city scale. The results indicated that Pudong District had seen the highest number of positive change patches and the highest degree of change areas. On the contrary, Jinshan District has the lowest number of positive change patches number and the lowest degree of change areas. This is following development planning (Qiu and Xu, 2017). The year 2015 was the end of the "12 th Five-Year Plan", and 2016 was the beginning of the "13 th Five-Year Plan". Pudong District aimed at coordination, green, openness, and sharing and was striving for steady economic development as it was the focus of Shanghai's future development. A particular advantage of our proposed method is that we can locate each positive change at the meter level. We can therefore identify land use type and specific changes from POI data such as Google street view. This is a new joint perspective to understand PUD dynamics better.

From the local policy perspective, we can justify the motivation for the detected positive changes. Traditionally, the producer services are considered to be clustered and located in the city center to benefit from agglomeration effects (Wei et al., 2016). Because of the development of information and communication technology, the location of the software industry has changed to reflect a polycentric pattern. Correspondingly, the detected Sanlin software park is located outside the CBD or the sub-CBD area in Pudong District. The dynamic spatial pattern of the software industry is influenced mainly by government decisions, e.g., the location of CBDs, development zones, and new towns (Wei et al., 2016), while the intra-urban level, agglomeration, accessibility, environment status, and accommodation-related factors are critical in selecting the software industry location (Yi et al., 2011). Such factors can be explored further to explain the detected changes and from different perspectives of PUD dynamics.

5. Conclusions

This study, for the first time, demonstrated the potential of using Sentinel-1 SAR imagery for polycentric urban development monitoring. Our study consolidated the role of SAR imagery in embedding it into the high spatio-temporal PUD framework. Using our proposed KI-MM change detection methods, we detected 2526, 2409, and 4232 newly built-up positive-changed patches, with areas equal to 18, 20, 36 km², respectively. These changes are associated with the polycentricity development in Shanghai between 2015 and 2018. Validated with the optical reference observations, Sentinel-1A/B offers reliable observations as the average matching rates for the positive changed areas were equal to 89.79%, 100%, and 88.64% between 2015 and 2018, while the F1-scores were 91.67%, 100%, and 94.06%, respectively. We proposed two polycentricity indicators, i.e., the mean distance and the patch area. These two indicators can help us recognize the spatial relation between newly built-up patches and their spatial structure. For instance, the observed 888 m mean distance of all validation sites

implied a close distance of all newly built-up patches, while a potential new city center is rising in the vicinity. In addition, we tested 80 distribution models and sought out the optimized one to derive objective and steady threshold values. The convolution kernel filtering in space and variance-based temporal filtering reduced the noise while retaining the original information of the signal. Compared with traditional PUD data sources, e.g., LandScan data, we demonstrated that employing satellite SAR data can detect building changes at higher spatial and temporal resolutions. We can detect the new-born city centers at the meter resolution, and associate the centers with local policies. Furthermore, employing our method for any other designated sites is straightforward, as our method is based on the statistical property of the images rather than the location of the study area. In the future, we will further explore the negative changed patches and their link with PUD.

CRediT authorship contribution statement

Xu Zhang: Methodology, Software, Formal analysis, Investigation, Data curation, Writing – original draft, Visualization. **Ling Chang:** Conceptualization, Methodology, Writing – review & editing, Supervision. **Mingshu Wang:** Conceptualization, Resources, Writing – review & editing. **Alfred Stein:** Writing – review & editing.

Declaration of competing interest

The authors declare that they have no known competing financial interests or personal relationships that could have appeared to influence the work reported in this paper.

Data availability

Data will be made available on request.

Acknowledgments

The authors would like to thank the European Space Agency for providing the archived Sentinel-1A/B SAR data and Sentinel-2 optical data, and Google Earth Engine for offering such a powerful cloud computing platform.

Appendix A. KI-MM equation derivation

We start from the conditional probability $e(X, T)$ of log-ratio map value X falling into different categories $c \in \{1, 2\}$ with a certain threshold T ,

$$e(X, T) = h(X|c, T)P_c(T)/h(X), \quad (\text{A.1})$$

where $h(X|c, T)$ is the best fitted distribution model, $P_c(T) = \sum h(X)$ is the *a priori* probability. In our test site, we found that Laplace is the best fitted model and the log-ratio map (N values in total and range between $[m, n]$) should follow the distribution $f(X|u, b) = \frac{1}{2b} \exp(-\frac{|X-u|}{b})$, where $b = \frac{1}{N} \sum_m |X - u|$.

As $h(X|c, T)$ is independent of both c and T , $h(X)$ can be ignored in the following derivation. To simplify the calculation, we take the logarithm of the numerator in Eq. (A.1) and multiply by -1 , and we get the

$$\begin{aligned} e(X, T) &= -1 \ln(h(X|c, T)P_c(T)) \\ &= -1 \ln(f(X|u_c, b_c)P_c(T)) \\ &= -1 \ln\left(\frac{1}{2b_c} \exp\left(-\frac{|X - u_c(T)|}{b_c}\right)P_c(T)\right) \\ &= -1(-\ln 2b_c - \frac{|X - u_c(T)|}{b_c} + \ln P_c(T)) \\ &= \ln 2b_c + \frac{|X - u_c(T)|}{b_c} - \ln P_c(T) \end{aligned} \quad (\text{A.2})$$

Table B.5

F1-score of nine validation sites.

Year	Validation sites	Positive changes (%)	Negative changes (%)	Stable (%)	Average (%)
2015–2016	A1	100	100	96.10	98.70
	A2	75	88.89	98.29	87.39
	A3	100	100	99.12	99.71
2016–2017	B1	100	100	97.56	99.19
	B2	100	92.31	97.15	96.49
	B3	100	96.55	99.10	98.55
2017–2018	C1	97.15	100	98.96	98.70
	C2	94.12	100	99.52	97.88
	C3	90.91	100	98.72	96.54
Average (%)		95.24	97.53	98.28	

Table C.6

Validation statistics of the nine validation sites using the Normal distribution. Here the columns for Positive changes, Negative changes, Stable and average, and last row for Average show the matching rate between Sentinel-1 and Sentinel-2 results with the units of %.

Year	Validation sites	Positive changes (%)	Negative changes (%)	Stable (%)	Average (%)
2015–2016	A1	79.91	100	86.54	88.82
	A2	37.31	71.72	96.75	68.59
	A3	100	100	94.75	98.25
2016–2017	B1	95.24	62.24	93.81	83.76
	B2	94.52	73.00	87.40	84.97
	B3	50.67	98.04	92.26	80.32
2017–2018	C1	89.04	96.28	95.91	93.74
	C2	100	100	92.54	97.51
	C3	90.95	93.42	91.68	92.02
Average (%)		81.96	88.30	92.40	

The criterion function of threshold T is defined as $J(T) = \sum h(X)\epsilon(X, T)$, and when we integrate it with Eq. (A.2), we get

$$\begin{aligned}
 J(T) &= \sum_m^T h(X)(\ln 2b_1 + \frac{|X - u_1(T)|}{b_1} - \ln P_1(T)) + \\
 &\quad \sum_n^T h(X)(\ln 2b_2 + \frac{|X - u_2(T)|}{b_2} - \ln P_2(T)) \\
 &= P_1 \ln 2b_1 + P_1(T) \sum_m^T \frac{|X - u_1(T)|}{b_1} - P_1(T) \ln(P_1(T)) \\
 &\quad + P_2 \ln 2b_2 + P_2(T) \sum_n^T \frac{|X - u_2(T)|}{b_2} - P_2(T) \ln(P_2(T))
 \end{aligned} \tag{A.3}$$

Appendix B. Accuracy metric: F1-score

F1-score is calculated using $F_1 = \frac{2 \cdot \text{precision} \cdot \text{recall}}{\text{precision} + \text{recall}}$, with $\text{precision} = \frac{TP}{TP + FP}$, and $\text{recall} = \frac{TP}{TP + FN}$. TP denoting the true positive in prediction, FP the false positive, FN the false negative, and TN the true negative. The F1-score value in Table B.5 is similar to the accuracy value calculated in Section 3.6.

Appendix C. KI threshold with the Normal distribution

Here, we make a comparison with different distribution models to show the efficiency of our method. Since some of the models, e.g., Generalized Gaussian, Nakagami ratio, and Weibull ratio, were not suitable in our case, we selected the Normal distribution, which is at the third place in our list of tested models in Figs. 5 (a)–(c).

Determining appropriate critical values for D_{LR} is important to distinguish between changed and non-changed areas. Using Eq. (3), the log-ratio map of SAR image stacks A and B, being a gray scale map, can be yielded. The histogram of this log-ratio map, $h(k)$, where k is the pixel's gray value in $[0, 255]$, is then equal to the mixture of changed or

unchanged areas, and a threshold value K_{KI} is chosen to separate these two. For the Normal distribution, the quality of a potential threshold value T changes to

$$J(T) = -2 \sum_k h(k) \ln \left[\frac{h(k|c, T) P_c(T)}{h(k)} \right], \tag{C.1}$$

The conditional probability $h(k|c, T)$ is assumed to be Normally distributed. A value of $c = 1$ represents the class of unchanged pixels ($k < K_{KI}$), while $c = 2$ represents the class of changed pixels ($k > K_{KI}$). Eq. (C.1) is reformulated by integrating the two classes,

$$\begin{aligned}
 J(T) &= 1 + 2[P_1(T) \ln(\sigma_1(T)) + P_2(T) \ln(\sigma_2(T))] \\
 &\quad - 2[P_1(T) \ln(P_1(T)) + P_2(T) \ln(P_2(T))],
 \end{aligned} \tag{C.2}$$

where $\sigma_1(T)$ and $\sigma_2(T)$ are the standard deviations for the two classes.

Validation maps are shown in Fig. C.10 and the corresponding validation statistics in Table C.6. We saw that more pseudo changed patches are detected, for example, the positive changes shown in the top right of Fig. C.10(b). The incorrectly detected patches lead to lower accuracy in the A2 row and positive changes column of Table C.6. This is similar to other test sites. Besides, employing the KI threshold with Normal distribution, the numbers of patches with positive and negative changes occupy 25.76%, 18.64%, and 20.33% of total detected patches, and their area makes up 29.22%, 19.94%, and 24.08%, respectively. When using the KI-MM threshold values, their numbers of patches occupy 8.38%, 6.51%, and 5.74%, their areas make up 13.74%, 10.22%, and 10.77%, respectively. The improper Normal distribution model brings more falsely detected patches, extends the patch boundary, and merges patches, leading to a higher proportion of patch number and area. It shows as expected that the change detection thresholds produced by the best-fitted model are more reliable. In general, the performance of the Normal distribution is poor w.r.t the Laplace distribution.

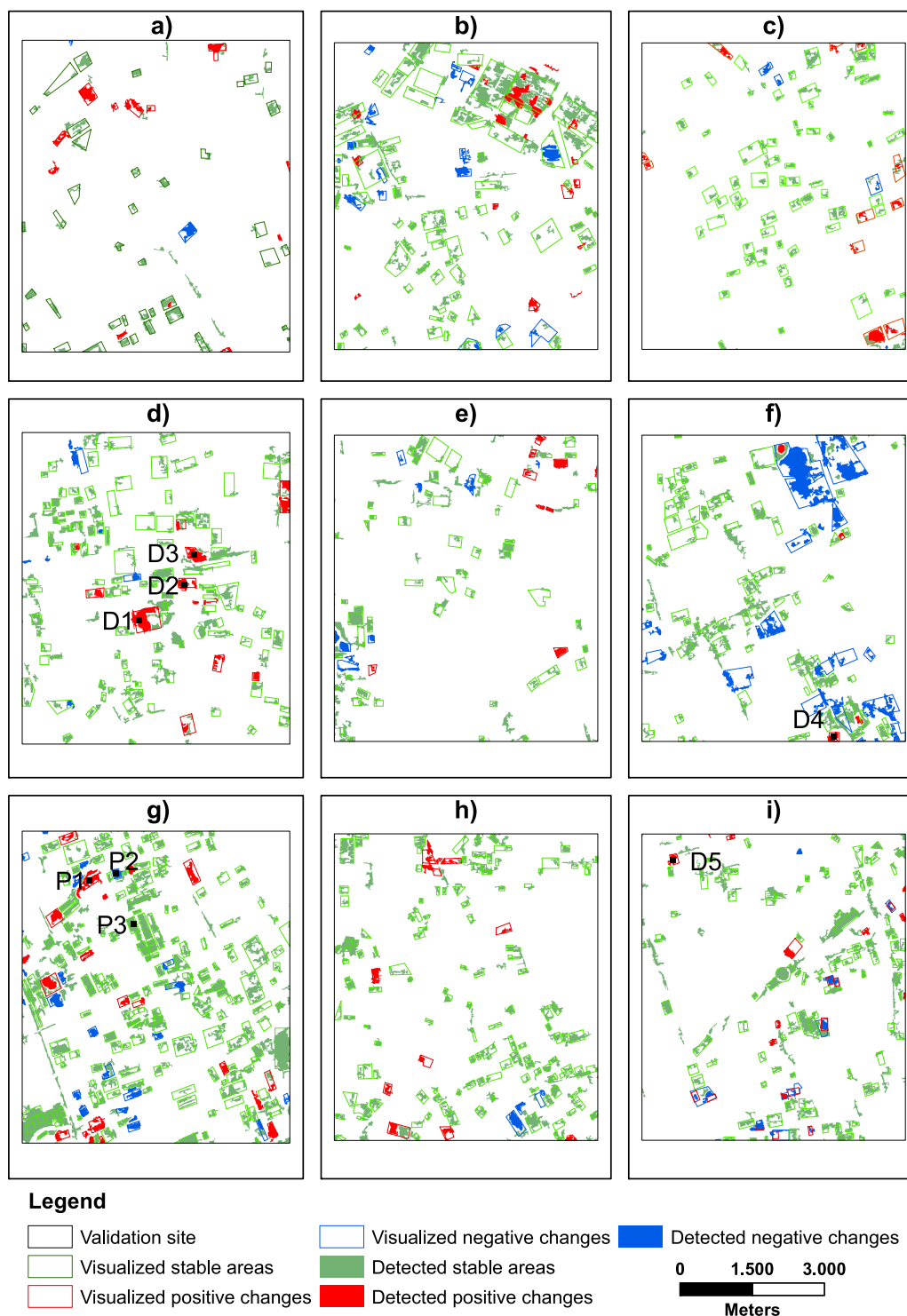


Fig. C.10. Validation maps of sites A1 (a), A2 (b), A3 (c), between 2015 and 2016, and B1 (d), B2 (e), B3 (f) between 2016 and 2017, and C1 (g), C2 (h), C3 (i) between 2017 and 2018 using the Normal distribution.

References

- Ashok, A., Rani, H.P., Jayakumar, K., 2021. Monitoring of dynamic wetland changes using NDVI and NDWI based landsat imagery. *Remote Sens. Appl.: Soc. Environ.* 23, 100547.
- Bailey, N., Turok, I., 2001. Central Scotland as a polycentric urban region: useful planning concept or chimera? *Urban Stud.* 38 (4), 697–715.
- Ban, Y., Yousif, O.A., 2012. Multitemporal spaceborne SAR data for urban change detection in China. *IEEE J. Sel. Top. Appl. Earth Obs. Remote Sens.* 5 (4), 1087–1094.
- Bhaduri, B., Bright, E., Coleman, P., Urban, M.L., 2007. LandScan USA: a high-resolution geospatial and temporal modeling approach for population distribution and dynamics. *GeoJournal* 69 (1), 103–117.
- Cai, J., Huang, B., Song, Y., 2017. Using multi-source geospatial big data to identify the structure of polycentric cities. *Remote Sens. Environ.* 202, 210–221.
- Chen, Y., 2014. Shanghai city strategy 2050: road map to knowledge city. In: *Urban Futures Squaring Circles: Proceedings, International Conference on Urban Futures Squaring Circles*, Vol. 2050.
- Chen, X., Chen, X., Song, M., 2021. Polycentric agglomeration, market integration and green economic efficiency. *Struct. Change Econ. Dyn.* 59, 185–197.

- Derudder, B., Liu, X., Wang, M., Zhang, W., Wu, K., Caset, F., 2021. Measuring polycentric urban development: The importance of accurately determining the 'balance' between 'centers'. *Cities* 111, 103009.
- Dobson, J.E., Bright, E.A., Coleman, P.R., Durfee, R.C., Worley, B.A., 2000. LandScan: a global population database for estimating populations at risk. *Photogramm. Eng. Remote Sens.* 66 (7), 849–857.
- Fang, H., Du, P., Wang, X., 2022. A novel unsupervised binary change detection method for VHR optical remote sensing imagery over urban areas. *Int. J. Appl. Earth Obs. Geoinf.* 108, 102749.
- Gong, M., Cao, Y., Wu, Q., 2011. A neighborhood-based ratio approach for change detection in SAR images. *IEEE Geosci. Remote Sens. Lett.* 9 (2), 307–311.
- Gorelick, N., Hancher, M., Dixon, M., Ilyushchenko, S., Thau, D., Moore, R., 2017. Google Earth Engine: Planetary-scale geospatial analysis for everyone. *Remote Sens. Environ.* 202, 18–27.
- Hajrasouliha, A.H., Hamidi, S., 2017. The typology of the American metropolis: monocentricity, polycentricity, or generalized dispersion? *Urban Geogr.* 38 (3), 420–444.
- Hall, P.G., Pain, K., 2006. *The Polycentric Metropolis: Learning from Mega-City Regions in Europe*. Routledge.
- Hu, H., Ban, Y., 2014. Unsupervised change detection in multitemporal SAR images over large urban areas. *IEEE J. Sel. Top. Appl. Earth Obs. Remote Sens.* 7 (8), 3248–3261.
- Kittler, J., Illingworth, J., 1986. Minimum error thresholding. *Pattern Recognit.* 19 (1), 41–47.
- Kittler, J., Illingworth, J., Foglein, J., Paler, K., 1984. Automatic thresholding algorithm and its performance. In: *Proceedings-International Conference on Pattern Recognition*. pp. 287–289.
- Kumar, V., Mandal, D., Bhattacharya, A., Rao, Y., 2020. Crop characterization using an improved scattering power decomposition technique for compact polarimetric SAR data. *Int. J. Appl. Earth Obs. Geoinf.* 88, 102052.
- Kuruoglu, E.E., Zerubia, J., 2004. Modeling SAR images with a generalization of the Rayleigh distribution. *IEEE Trans. Image Process.* 13 (4), 527–533.
- Li, Y., Derudder, B., 2020. Dynamics in the polycentric development of Chinese cities, 2001–2016. *Urban Geogr.* 1–21.
- Li, Y., Derudder, B., 2022. Dynamics in the polycentric development of Chinese cities, 2001–2016. *Urban Geogr.* 43 (2), 272–292.
- Lin, P.-H., Chen, B.-H., Cheng, F.-C., Huang, S.-C., 2016. A morphological mean filter for impulse noise removal. *J. Disp. Technol.* 12 (4), 344–350.
- Liu, C., Chen, Z., Yun, S., Chen, J., Hasi, T., Pan, H., 2019. Research advances of SAR remote sensing for agriculture applications: A review. *J. Integr. Agric.* 18 (3), 506–525.
- Liu, X., Derudder, B., Wang, M., 2018. Polycentric urban development in China: A multi-scale analysis. *Environ. Plan. B: Urban Anal. City Sci.* 45 (5), 953–972.
- Liu, X., Wang, M., 2016. How polycentric is urban China and why? A case study of 318 cities. *Landsc. Urban Plan.* 151, 10–20.
- Liu, X., Wang, M., Qiang, W., Wu, K., Wang, X., 2020. Urban form, shrinking cities, and residential carbon emissions: Evidence from Chinese city-regions. *Appl. Energy* 261, 114409.
- Liu, Z., Zhang, A., Yao, Y., Shi, W., Huang, X., Shen, X., 2021. Analysis of the performance and robustness of methods to detect base locations of individuals with geo-tagged social media data. *Int. J. Geogr. Inf. Sci.* 35 (3), 609–627.
- Ma, J., Gong, M., Zhou, Z., 2012. Wavelet fusion on ratio images for change detection in SAR images. *IEEE Geosci. Remote Sens. Lett.* 9 (6), 1122–1126.
- McMillen, D.P., 2001. Nonparametric employment subcenter identification. *J. Urban Econ.* 50 (3), 448–473.
- Meng, M., Shang, Y., Yang, Y., 2021. Did highways cause the urban polycentric spatial structure in the Shanghai metropolitan area? *J. Transp. Geogr.* 92, 103022.
- Morshed, M.M., Mazumder, T., Sarkar, S.K., Sami, F.Y., Ishra, A.K., Sydnunaher, S., 2022. Transformation towards a mega-regional formation of Khulna city, Bangladesh. *Spatial Inf. Res.* 30 (5), 665–677.
- Moser, G., Serpico, S.B., 2006. Generalized minimum-error thresholding for unsupervised change detection from SAR amplitude imagery. *IEEE Trans. Geosci. Remote Sens.* 44 (10), 2972–2982.
- Murakami, J., Chang, Z., 2018. Polycentric development under public leasehold: A spatial analysis of commercial land use rights. *Reg. Sci. Urban Econ.* 71, 25–36.
- Nakagawa, Y., Rosenfeld, A., 1979. Some experiments on variable thresholding. *Pattern Recognit.* 11 (3), 191–204.
- Puttanapong, N., Luenam, A., Jongwattanakul, P., 2022. Spatial analysis of inequality in Thailand: Applications of satellite data and spatial statistics/econometrics. *Sustainability* 14 (7), 3946.
- Qiu, R., Xu, W., 2017. Modes of land development in Shanghai. *Land Use Policy* 61, 475–486.
- Rubel, O., Lukin, V., Rubel, A., Egiazarian, K., 2021. Selection of Lee filter window size based on despeckling efficiency prediction for sentinel SAR images. *Remote Sens.* 13 (10), 1887.
- Sofiane, H., Ferdaous, C., 2010. Comparison of change detection indicators in SAR images. In: *8th European Conference on Synthetic Aperture Radar*. VDE, pp. 1–4.
- Sun, T., Lv, Y., 2020. Employment centers and polycentric spatial development in Chinese cities: A multi-scale analysis. *Cities* 99, 102617.
- Szabo, S., Gácsi, Z., Balazs, B., 2016. Specific features of NDVI, NDWI and MNDWI as reflected in land cover categories. *Landsc. Environ.* 10 (3–4), 194–202.
- Tamiminia, H., Salehi, B., Mahdianpari, M., Quackenbush, L., Adeli, S., Brisco, B., 2020. Google Earth Engine for geo-big data applications: A meta-analysis and systematic review. *ISPRS J. Photogramm. Remote Sens.* 164, 152–170.
- Van Nuffel, N., Saey, P., Derudder, B., Devriendt, L., Witlox, F., 2010. Measuring hierarchical differentiation: connectivity and dominance in the European urban network. *Transp. Plan. Technol.* 33 (4), 343–366.
- Virtanen, P., Gommers, R., Oliphant, T.E., Haberland, M., Reddy, T., Cournapeau, D., Burovski, E., Peterson, P., Weckesser, W., Bright, J., van der Walt, S.J., Brett, M., Wilson, J., Millman, K.J., Mayorov, N., Nelson, A.R.J., Jones, E., Kern, R., Larson, E., Carey, C.J., Polat, İ., Feng, Y., Moore, E.W., VanderPlas, J., Laxalde, D., Perktold, J., Cimrman, R., Henriksen, I., Quintero, E.A., Harris, C.R., Archibald, A.M., Ribeiro, A.H., Pedregosa, F., van Mulbregt, P., SciPy 1.0 Contributors, 2020. SciPy 1.0: Fundamental algorithms for scientific computing in Python. *Nature Methods* 17, 261–272. <http://dx.doi.org/10.1038/s41592-019-0686-2>.
- Wan, L., Xiang, Y., You, H., 2019. An object-based hierarchical compound classification method for change detection in heterogeneous optical and SAR images. *IEEE Trans. Geosci. Remote Sens.* 57 (12), 9941–9959.
- Wang, M., 2021. Polycentric urban development and urban amenities: Evidence from Chinese cities. *Environ. Plan. B: Urban Anal. City Sci.* 48 (3), 400–416.
- Wang, M., Debbage, N., 2021. Urban morphology and traffic congestion: Longitudinal evidence from US cities. *Comput. Environ. Urban Syst.* 89, 101676.
- Wang, M., Derudder, B., Liu, X., 2019. Polycentric urban development and economic productivity in China: A multiscale analysis. *Environ. Plan. A: Econ. Space* 51 (8), 1622–1643.
- Wei, Y.D., Bi, X., Wang, M., Ning, Y., 2016. Globalization, economic restructuring, and locational trajectories of software firms in Shanghai. *Prof. Geogr.* 68 (2), 211–226.
- Wei, L., Luo, Y., Wang, M., Cai, Y., Su, S., Li, B., Ji, H., 2020. Multiscale identification of urban functional polycentricity for planning implications: An integrated approach using geo-big transport data and complex network modeling. *Habitat Int.* 97, 102134.
- Wu, C., Smith, D., Wang, M., 2021. Simulating the urban spatial structure with spatial interaction: A case study of urban polycentricity under different scenarios. *Comput. Environ. Urban Syst.* 89, 101677.
- Xie, J., Ren, C., Li, X., Chung, L.C.H., 2022. Investigate the urban growth and urban-rural gradients based on local climate zones (1999–2019) in the Greater Bay Area, China. *Remote Sens. Appl.: Soc. Environ.* 25, 100669.
- Yi, H., Yang, F.F., Yeh, A.G., 2011. Intraurban location of producer services in Guangzhou, China. *Environ. Plan. A* 43 (1), 28–47.
- Zhang, T., Sun, B., Li, W., Dan, B., Wang, C., 2019. Polycentricity or dispersal? The spatial transformation of metropolitan Shanghai. *Cities* 95, 102352.
- Zhao, X., Liu, Y., Pang, X., Ji, Q., Stein, A., Cheng, X., Chen, Y., 2022. Concept-driven extraction of the Antarctic marginal sea ice zone from remote sensing image time series. *Spatial Stat.* 100578.